ARMY RESEARCH LABORATORY

Finite-Element Micromechanical Strength Modeling and Parametric Investigation of Three-Dimensional Orthogonal Composites

by Ryan L. Karkkainen and Jerome T. Tzeng

ARL-TR-4355 **January 2008**

NOTICES

Disclaimers

The findings in this report are not to be construed as an official Department of the Army position unless so designated by other authorized documents.

Citation of manufacturer's or trade names does not constitute an official endorsement or approval of the use thereof.

Destroy this report when it is no longer needed. Do not return it to the originator.

Army Research Laboratory
Aberdeen Proving Ground, MD 21005-5069

ARL-TR-4355 **January 2008**

Finite-Element Micromechanical Strength Modeling and Parametric Investigation of Three-Dimensional Orthogonal Composites

Ryan L. Karkkainen
Oak Ridge Institute for Science and Education

Jerome T. Tzeng
Weapons and Materials Research Directorate, ARL

REPORT DOCUMENTATION PAGE	Form Approved OMB No. 0704-0188

1. REPORT DATE *(DD-MM-YYYY)*	2. REPORT TYPE	3. DATES COVERED (From - To)
January 2008	Final	June 2006–November 2007

4. TITLE AND SUBTITLE
Finite-Element Micromechanical Strength Modeling and Parametric Investigation of Three-Dimensional Orthogonal Composites

5a. CONTRACT NUMBER

5b. GRANT NUMBER

5c. PROGRAM ELEMENT NUMBER

6. AUTHOR(S)
Ryan L. Karkkainen* and Jerome T. Tzeng

5d. PROJECT NUMBER
622618H75

5e. TASK NUMBER

5f. WORK UNIT NUMBER

7. PERFORMING ORGANIZATION NAME(S) AND ADDRESS(ES)
U.S. Army Research Laboratory
ATTN: AMSRD-ARL-WM-MB
Aberdeen Proving Ground, MD 21005-5069

8. PERFORMING ORGANIZATION REPORT NUMBER
ARL-TR-4355

9. SPONSORING/MONITORING AGENCY NAME(S) AND ADDRESS(ES)

10. SPONSOR/MONITOR'S ACRONYM(S)

11. SPONSOR/MONITOR'S REPORT NUMBER(S)

12. DISTRIBUTION/AVAILABILITY STATEMENT
Approved for public release; distribution is unlimited.

13. SUPPLEMENTARY NOTES
*Postdoctoral fellow through the Oak Ridge Institute for Science and Education, Aberdeen Proving Ground, MD 21005

14. ABSTRACT
Three-dimensional (3-D) reinforcement is often employed in thick composite parts to increase delamination resistance and through-thickness properties. Such materials are of particular interest for employment as insulators for the composite electromagnetic railgun insulator, which exhibits delamination as its primary failure mode. In the current study, a 3-D orthogonal woven S2-glass composite is investigated using finite-element micromechanics to characterize and evaluate its potential use in this target application. The representative volume element (RVE) of the 3-D woven microstructure is modeled directly through the 3-D finite-element model. Direct modeling of the exact microstructure allows for precise knowledge of the mechanics and failure modes of the microstructure under various loading conditions. Stiffness and strength are determined using a series of simulated characterization tests upon the RVE, with a detailed analysis of the resulting microstress field. Modeling results are verified by comparing experimental data. Tensile tests and Iosipescu shear tests have been performed to determine in-plane and transverse shear properties. Off-axis tensile tests were performed for further model validation. In-plane stiffness and strength were predicted with 90% or better accuracy. Transverse shear properties were less well predicted, but strength was still predicted within 86% accuracy. The micromechanical methods were then employed towards a parametric study of the effect of stitch density on promising improvement of delamination resistance and shear properties, as well as consequent loss of in-plane properties.

15. SUBJECT TERMS
textile reinforcement, micromechanics, composites, 3-D woven, micromechanics

16. SECURITY CLASSIFICATION OF:			17. LIMITATION OF ABSTRACT	18. NUMBER OF PAGES	19a. NAME OF RESPONSIBLE PERSON
a. REPORT	b. ABSTRACT	c. THIS PAGE			Jerome T. Tzeng
UNCLASSIFIED	UNCLASSIFIED	UNCLASSIFIED	UL	34	19b. TELEPHONE NUMBER (*Include area code*) 410-306-0959

Contents

List of Figures

List of Tables

Acknowledgments

This project was supported in part by the Research Participation Program for the U.S. Army Research Laboratory (ARL) administered by the Oak Ridge Institute for Science and Education through an agreement between the U.S. Department of Energy and ARL. Also, the authors would like to express their appreciation to Drs. Shridhar Yarlagadda and John (Jack) Gillespie for their efforts in three-dimensional composite manufacturing under the sponsorship of the U.S. Army Composite Material Technology program at the University of Delaware.

INTENTIONALLY LEFT BLANK.

1. Introduction

Three-dimensional (3-D) textile composites offer key benefits to structural robustness for applications involving impact, multidimensional loading or thick sections with relatively large through-thickness or delamination stresses. Such is also the case for any two-dimensional (2-D) woven or braided composite structures, which inherently provide reinforcement in multiple directions and may include some out-of-plane reinforcement by nature of the undulation of interwoven fiber tows. However, the 3-D orthogonal weave incorporates fiber tows directly in the through-thickness direction. This is critical to delamination resistance, an otherwise common weak point of thick composite structures. Consequently, this also leads to loss of in-plane properties compared to a 2-D or laminated structure of the same fiber volume fraction, as the stitches lead to interruption of in-plane fiber tows and loss of volume fraction of fibers aligned to resist in-plane loading.

The increased microstructural complexity of textile composites also leads to increased complexity of characterization and analysis as well as a need for nontraditional analysis methods. The benefits in performance and manufacturability can outweigh these drawbacks with effective design and knowledge of the micromechanical response, as appropriate to the particular application being considered.

An accurate model must accommodate the fact that 3-D woven composites exhibit multiple potential failure mechanisms (*1*), which depend upon the loading conditions and particulars of the layup and materials. Three-dimensional weaves consistently show improved damage resistance over their 2-D counterparts due to the energy absorbing capacity enhanced by the *z*-direction fiber tows (*2*, *3*). Three-dimensional weaves also show more capacity to absorb multiple strikes before perforation and show less damage localization (*4*). This can be of particular interest in armor applications, and related modeling has addressed issues surrounding the computational needs required to reflect the energy absorption modes and damage progression (*5*).

In addition to the improvement of impact performance, the effects of *z*-stitching upon shear properties have been shown experimentally, with increased delamination resistance and significantly increased compression-after-impact (CAI) capacity (*6*, *7*). Failure modes are shown to vary, dependent on the particulars of the textile architecture, especially with regards to CAI.

Designs of current textile composite structures are often based upon well-known phenomenological failure criterion, predominantly the maximum stress criterion, maximum strain criterion, and quadratic interaction criterion, such as the Tsai-Hill and Tsai-Wu failure theories (*8*, *9*). Dedicated analysis of 2-D and 3-D textile composites has been approached before (*10*–*16*); however, effective strength prediction is still a topic of much current study and development.

Finite-element model (FEM) micromechanical methods for strength modeling of textile composites have been explored in previous works (*17–19*). This employed a method, known as the Direct Micromechanics Method (*20*, *21*), to develop failure envelopes and a quadratic stress gradient failure theory for a plain-weave textile composite. Therein, it was shown that the microlevel scale of a textile composite is physically larger and geometrically more complex than a unidirectional composite. Thus, many common assumptions and traditional micromechanical analysis techniques break down. Improvements to these techniques have been presented towards effective failure prediction under complex loading conditions.

Three-dimensional woven composites show solid potential for use in improving delamination resistance and impact resistance in a lightweight material, which can be important in armor or structural applications. In particular, with the electromagnetic railgun launcher, significant electromagnetic forces generated in the aluminum rail sections can lead to delamination of the insulator materials, currently a filament-wound S2 glass – BMI composite. Therefore, investigation is made into the delamination resistance potential of composites with 3-D reinforcement. The current work involves applying FEM micromechanics to the 3-D orthogonal weave to provide detailed stiffness and strength modeling for failure prediction. Experimental analysis of multiple specimen types has been performed to provide model verification. The established micromechanical model is then applied towards a parametric study of the effects of variation in stiffness and strength for various stitch densities, which is used to illustrate the material's potential and provide guidelines for microstructural optimization.

2. Methods

Finite-element (FE) based micromechanical analysis has been performed to determine the stiffness and strength of a 3-D orthogonal weave textile composite. Once characterization simulations have been performed within the material model, FE stress-field outputs become the basis for an analytical model which can predict failure under arbitrary loading conditions. This then allows for a parametric study in which the properties of various 3-D orthogonal fiber microarchitectures can be investigated towards determination of an optimal geometry.

2.1 Representative Volume Element (RVE) Development

In terms of structural layout and dimensional accuracy, an extensive series of photomicrographs was taken to ensure the precise representation of the microstructure in the FEM. Specimens were cut in several planes of the 3-D orthogonal source plaque at various magnifications, with a length scale attached by the photomicrograph software. Figure 1 shows a picture taken in the *x*-*y* plane (a top view) from which multiple dimensions can be ascertained, such as stitch cross-section, stitch spacing, in-plane tow width, etc. The photo of figure 2 is taken in the *y*-*z* plane (a side view),

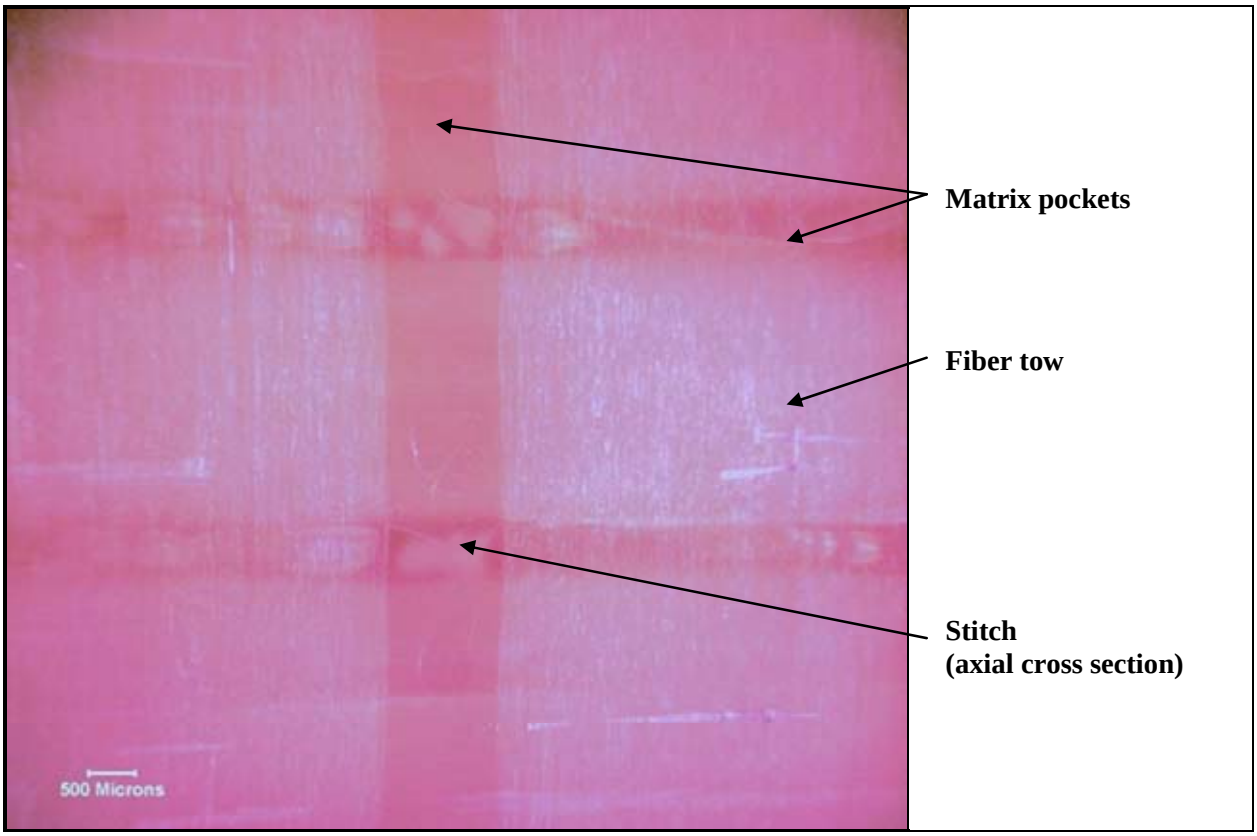

Figure 1. Photomicrograph in the *x-y* plane.

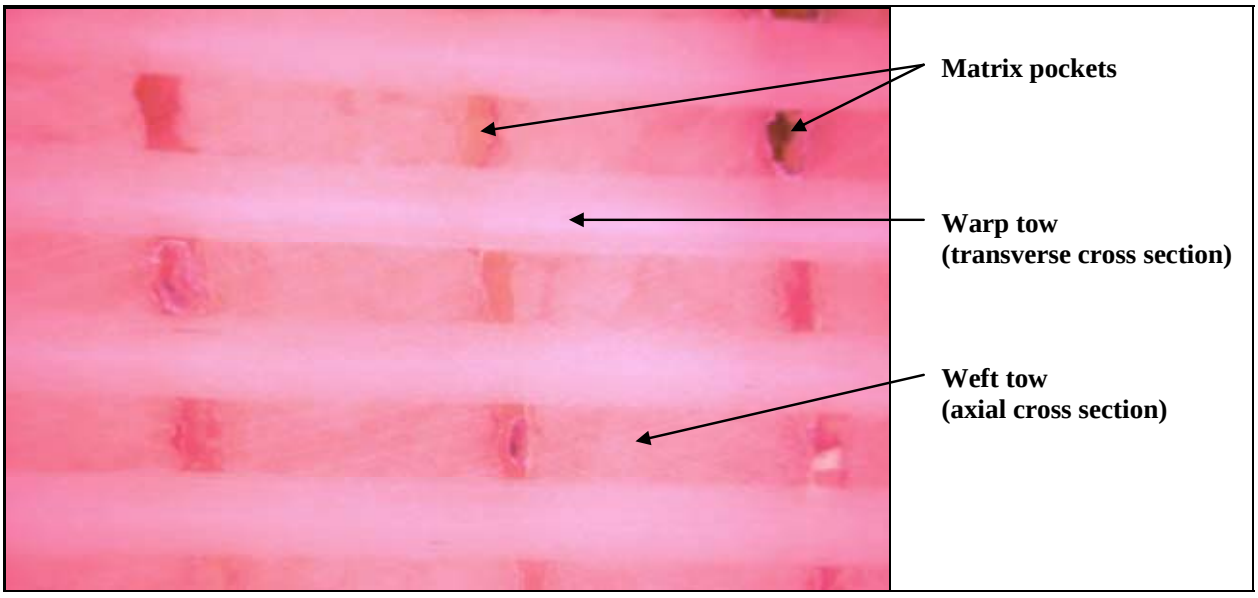

Figure 2. Photomicrograph in the *y-z* plane.

which illustrates the warp and weft tow heights, as well as multiple matrix pockets in areas where tows cannot be strung or woven (in this case, due to the interference of stitching). Further pictures not shown here were also taken to complete the microarchitectural and dimensional determination as well as to provide assurance of consistency of dimensions at multiple locations along the material plaque. Figure 3 provides a postburnout photomicrograph for which all resin material has been removed by residence in a high-temperature furnace. This is done to ensure proper distinction of the tow and matrix phases as well as to provide an accurate measure of the total fiber volume fraction. These pictures are not used to determine dimensions, as some drift of the fiber tows will occur while not contained in the binding resin matrix (some bowing of the tows can be seen in figure 3, which does not occur in the cured, resin-impregnated structure).

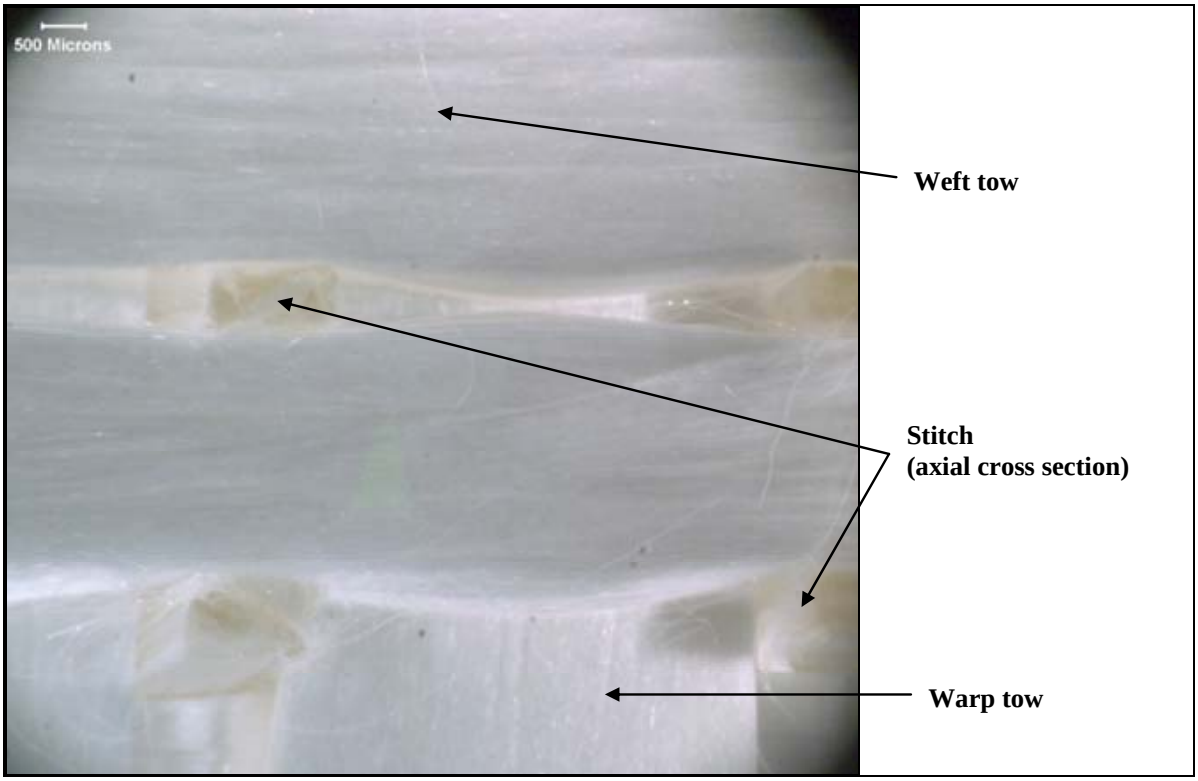

Figure 3. Photomicrograph in the *x*-*y* plane after resin matrix burnout.

Figure 4 shows one of several photomicrographs taken at higher magnification to investigate some of the subtleties of the microarchitecture. Fiber kinking, which is sometimes a concern for textile composites, is seen to be minimal or negligible. Further, even at this high magnification, the orthogonality of tows is quite evident. In fact, there is surprisingly little "blunting" or rounding at the corner points at which tows press against neighboring tows. Whereas, for textile composites, in general, loss of ideal geometry can sometimes be seen in the postprocessing (or postmanufacture) fiber structure, especially when the fiber preform is draped over a part or mold (though, in this case, the source material is a straight plaque).

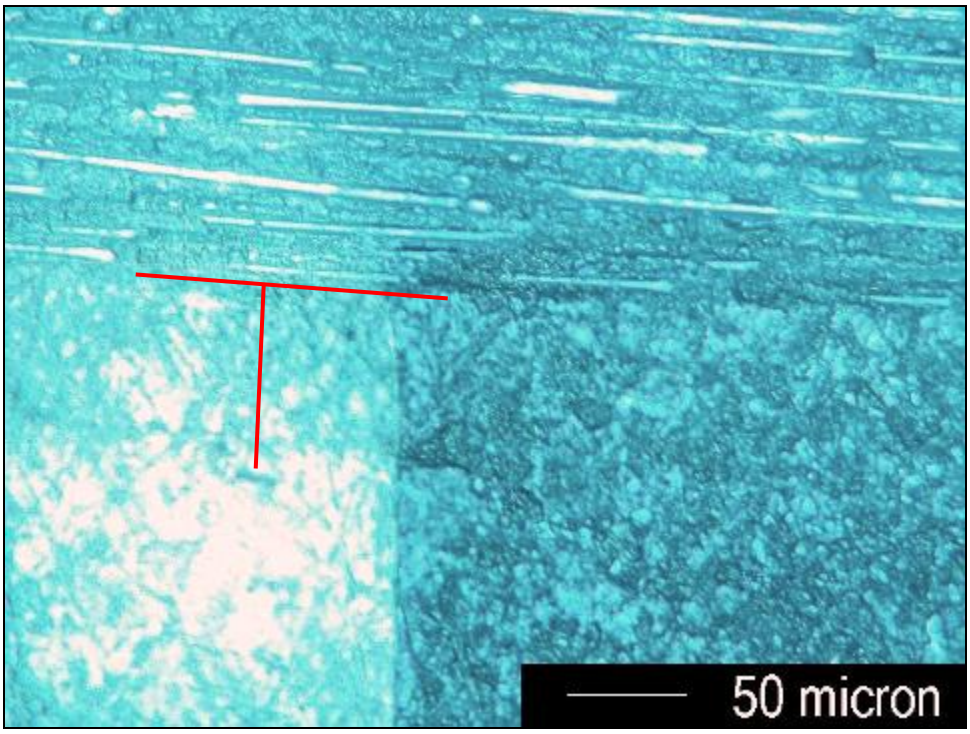

Figure 4. High magnification photomicrograph illustrating orthogonality of tows.

The smallest repeatable RVE of the textile architecture under investigation is shown in figure 5, with dimensions listed in table 1. Constituent properties are shown in tables 2 and 3 (note that fiber tows have the properties of an orthogonal composite at the micro or element level). In figure 5, the "warp" tows represent fiber tows for which the fibers run in the direction of the x-axis. "Weft" tows represent those for which fibers run in the y-direction. Unlike microgeometry such as the 2-D plain weave, there is no undulation or interweaving of the fiber tows (though such 3-D architectures do exist). Thus, each contributes its strength fully to the in-plane properties of the composite, while z-direction tows or stitches are placed to provide through-thickness properties. During fabrication of the 3-D orthogonal preform, small gaps subject to the limitations of the inter-strung fiber tow exist. Thus, some areas of interstitial matrix will be present (also indicated in figure 5). Given these interstitial gaps as well as the inherent volume fraction of resin-impregnated fiber tows, the overall volume fraction of the current RVE is 54%.

2.2 Modeling for Stiffness Prediction

The RVE is subjected to individual macroscopic (or RVE-level) displacements utilizing periodic boundary conditions which correspond to unit-strain along each axis. Each independently applied unit-strain results in a complete microlevel (or element-level) stress field comprised of

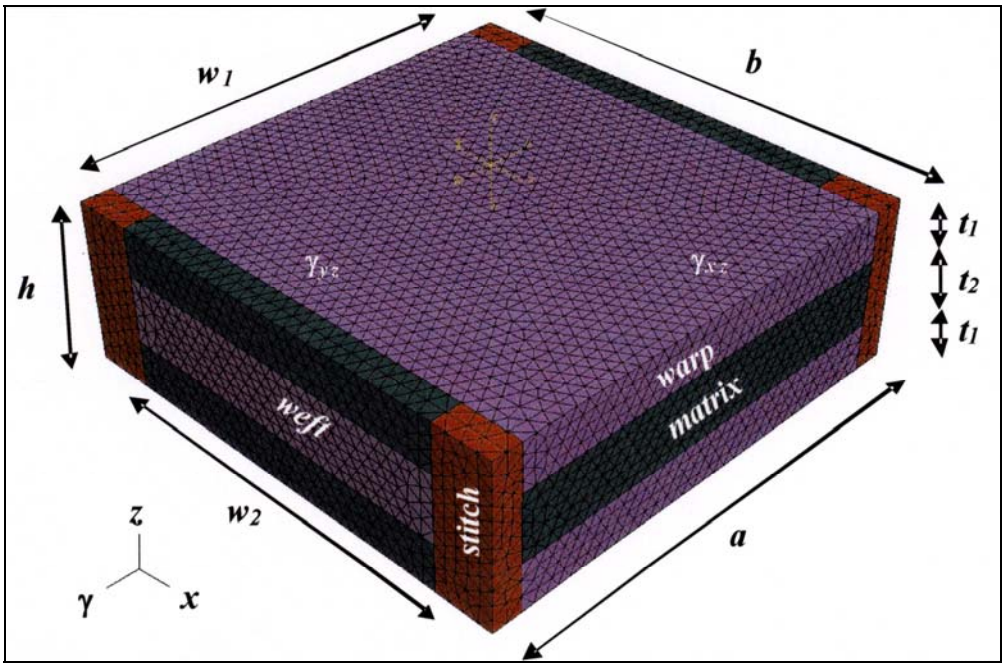

Figure 5. RVE geometry.

Table 1. RVE dimensions.

Dimension (mm)	Description	Value (mm)
a	RVE width	7.25
b	RVE depth	6.0
h	RVE height	1.68
t_1	Warp (half) thickness	0.49
t_2	Weft thickness	0.70
w_1	Warp width	6.62
w_2	Weft width	4.75

Table 2. Fiber tow and matrix material properties.

Material	E_1 (GPa)	E_2 (GPa)	G_{12} (GPa)	ν_{12}
S2 glass composite (65% fiber volume)	71.1	16.2	6.46	0.25
Neat resin	4.60	4.60	1.76	0.31

Table 3. Fiber tow and matrix strength properties.

Material	$S_L^{(+)}$ (MPa)	$S_L^{(-)}$ (MPa)	$S_T^{(+)}$ (MPa)	$S_T^{(-)}$ (MPa)	S_{LT} (MPa)
S2 glass composite	1705	550	45	150	50
Neat resin	103	103	103	103	—

the 3-D stresses in each element. The RVE is then characterized by analysis of the macrolevel stresses across the entire RVE, which are calculated by weighted averaging of the microstresses across the RVE volume. By applying known independent unit strain cases and evaluating the resulting macrostresses, one can completely determine the constitutive matrix. In this approach, structural stiffness coefficients are computed directly from the micromechanical models, and no underlying assumptions or approximations are needed.

The RVE is subjected to macroscopic stresses (σ) which are related to macroscopic strains (ε) according to the following equation:

$$[\sigma] = [C]\{\varepsilon\} \ . \tag{1}$$

The constitutive matrix [*C*] must be evaluated to define this correlation. To completely determine [*C*], a single unit strain is applied and all other deformation terms are set to zero in each of the cases shown in table 4. Displacements are applied using periodic boundary conditions. The periodic displacement boundary conditions isolate the mechanical effects of application of unit strains or curvatures and ensure the repeatability of deformations. Thus, the RVE is not only repeatable as a representative geometry, but is also mechanically repeatable in that each RVE has an identical response to strains and curvatures regardless of the location of that RVE in a textile plate or component. Note that displacements *u*, *v*, or *w* correspond to axial directions *x*, *y*, and *z*, respectively.

Table 4. Periodic displacement boundary conditions.

	u(b,y,z)-u(0,y,z)	***v(b,y,z)-v(0,y,z)***	***w(x,y,h)-w(x,y,0)***	***u(x,a,z)-u(x,0,z)***	***v(x,a,z)-v(x,0,z)***	***w(x,a,z)-w(x,0,z)***	***w(x,b,z)-w(x,0,z)***
$\varepsilon_x = 1$	b	0	0	0	0	0	0
$\varepsilon_y = 1$	0	0	0	0	a	0	0
$\varepsilon_z = 1$	0	0	h	0	0	0	0
$\gamma_{xy} = 1$	0	a/2	0	b/2	0	0	0
$\gamma_{xz} = 1$	0	0	0	0	0	b	0
$\gamma_{yz} = 1$	0	0	0	0	0	0	a

The FEM results for each element yield the microstresses resulting from an applied macrolevel strain. The corresponding macrolevel stress in each case can be computed by averaging the microstresses over the entire volume of the RVE as follows:

$$\sigma_{ij} = \left(1/_{abh}\right) \sum \sigma_{ij}^{e} V^{e} \ . \tag{2}$$

Here, *e* denotes summation over all elements in the FE model of the RVE, V^e is the volume of each element *e*, and *a*, *b*, and *h* are the dimensions of the RVE.

Thus, the constitutive relation of equation 1 can be found by independently evaluating the strain cases shown in table 4 and incorporating FEM results per equation 2. Each case will determine one column of the stiffness matrix [*C*], which is then completely defined once the results of all cases have been combined.

In order to then evaluate the stress state in the RVE resulting from any general applied load case, no further FEM analysis is necessary. The microstresses in each element can be extrapolated from the preliminary RVE analysis (just described) of each of the linearly independent macrostrain components. The microstress state for a general applied stress is obtained by superposing multiples of the results from the unit macrostrain analysis as follows:

$$\{\sigma^e\} = [F^e]\{\varepsilon\} \ . \tag{3}$$

Here, the 6×6 matrix $[F^e]$ contains the microstress in each element resulting from the unit strain analysis cases of table 4. For example, the microstress σ_y in the RVE for $\varepsilon_x = 0.05$ and $\varepsilon_y = 0.003$ is calculated as $\sigma_y = 0.05F_{21} + 0.003F_{25}$. Thus, further stress analyses are performed in an analytical model based upon superposition of the results of unit strain FEM analyses.

2.3 Strength Prediction

Strength can then be determined by evaluating the microstress field in the RVE resulting from any prescribed macrolevel force or stress. Strength is predicted by comparing the computed microstresses in each element against failure criteria for the constituent materials. Failure is checked on an element-by-element basis, and the failure criterion of each element can be selected appropriately based upon whether it is a tow or matrix element. For the isotropic matrix elements, the maximum principal stress criterion has been chosen to evaluate element failure. For fiber tow elements, the Tsai-Wu failure criterion is used, as this criterion is more suited to the orthotropic nature of the tows including stress interaction effects.

Failure envelopes (or simpler case-by-case failure analyses appropriate to an expected load set) are generated by first selecting a macrostress state to investigate. Then, the macrostrains and curvatures resulting from this applied loading are calculated from equation 1. Based on the scaled superposition of the results from FEM analysis of the unit load cases shown in table 4, the resulting stress field for the entire RVE is then calculated by equation 3. Failure is then checked in each element against a given failure criterion. This cycle is then repeated while progressively increasing a selected force or moment resultant and holding all others constant until an element level failure criterion is exceeded. If a particular failure criterion is exceeded, the element and the RVE are considered failures, which then defines the threshold of the failure envelope at a given point. Thus, failure envelopes for the textile composite can be generated in various force and moment resultant spaces.

2.4 Experimental Methods

Several experimental tests have been performed to verify the accuracy of stiffness and strength predictions via the micromechanics modeling. This establishes a baseline of veracity for the modeling and also establishes the material behavior in terms of linearity vs. nonlinearity, catastrophic vs. progressive failure, failure modes, etc. Two test sets have been performed—standard tensile tests to determine stiffness and strength in the axial directions and Iosipescu shear tests to determine in-plane and transverse shear stiffness and strength. To ensure repeatability and statistical certainty, each test is run for eight specimens. Tests are performed on a hydraulic mechanical testing system machine with a crosshead mounted load cell. Full-field strain measurements are obtained via the digital image correlation optical measurement technique. In this technique, a random speckle pattern is applied to the gauge section of the specimen. A pair of digital cameras then records a series of stereo images to track changes in the speckle pattern during testing. The images are postprocessed with image correlation software (*22*), which tracks the relative displacement of all speckles within the pattern and computes 3-D surface strains from these displacements.

In addition to the characterization tests, 30° and 45° off-axis specimens have been tested. These provide more challenging test cases for model validation, with a more complicated stress state. As shown in figure 6, standard uniaxial specimens are machined at 30° or 45° from the material axes of figure 5. When the specimen is loaded in tension, the stress state seen by the material (subscript "*mcs*" in equations 4 and 5) according to simple tensor change of axis transformation (*9*) indicates that axial, transverse, and shear stress will be present.

$$\tilde{\sigma}_{45} = \begin{Bmatrix} 1 \\ 0 \\ 0 \end{Bmatrix} \xrightarrow{tensor\_transform} \tilde{\sigma}_{mcs} = \begin{Bmatrix} 0.5 \\ 0.5 \\ 0.5 \end{Bmatrix} . \tag{4}$$

$$\tilde{\sigma}_{30} = \begin{Bmatrix} 1 \\ 0 \\ 0 \end{Bmatrix} \xrightarrow{tensor\_transform} \tilde{\sigma}_{mcs} = \begin{Bmatrix} 0.75 \\ 0.25 \\ 0.43 \end{Bmatrix} . \tag{5}$$

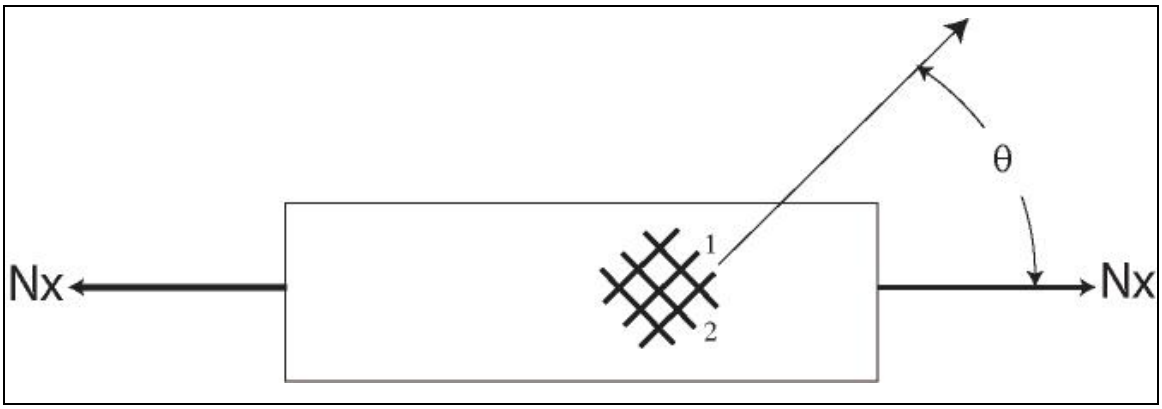

Figure 6. Schematic illustration of off-axis specimens loaded uniaxially with force N_x.

2.5 Parametric Modeling of Tow Microgeometry

Once the FEM micromechanical tools have been established and experimental results have validated the performance, the methods can then be extended to perform a parametric study of the effects of changes to microgeometry on mechanical performance. This becomes a powerful tool by which the effects of changes to microgeometry on the mechanical performance of the material can be quickly explored.

The chief driving force behind selection of a 3-D weave is to improve through-thickness properties, which are predominantly affected by the presence of the tows or stitches in the thickness direction. Thus, in the current study, the effects of variation in stitch density (the center-to-center distance between stitches, as indicated by the number of stitches per centimeter) is investigated, in terms of its consequence on improvement in transverse shear stiffness and strength, as well as through-thickness properties. Because in-plane properties can be adversely affected by the presence of stitching, this consequence is also explored.

Referring again to figure 5, the parametric study is performed by modifying the stitch spacing. In each case, a new RVE is created to reflect the new stitch density, and FE micromechanics are employed to determine the structural response. Increasing the RVE width and depth (dimensions *a* and *b*, respectively) corresponds to a lower stitch density and vice versa. Tow widths *w* are consequently affected as well, but all other dimensions remain the same. Four total stitch densities are investigated, as shown in table 5. Note that the material with zero-stitch density essentially amounts to a $[0/90/0]_s$ cross-ply laminate since only in-plane fibers in the *x* and *y* axial directions are present. Because the properties of the 3-D orthogonal structure can be compared to those of a cross-ply laminate, this provides a further basis upon which results may be gauged.

Table 5. Variation in RVE geometry for parametric study.

Name	Stitch Density (stitches/cm)	RVE Width (mm)	RVE Depth (mm)
Unstitched	0	9.0	9.0
Sparse	1.1	9.0	9.0
Baseline	1.5	7.25	6.0
Dense	2.0	5.0	5.0

Once the RVE geometry and mesh have been constructed, the methods of section 2.1 can then be reapplied for each new RVE in table 5. Displacements corresponding to in-plane and or transverse shear can be applied using periodic boundary conditions. The resulting stress field in each case, which now varies as the microgeometrical dimensions change, then relates the known displacement to the corresponding altered elastic constant. Also, per section 2.1, strength is again determined by evaluating the stress field on an element-by-element basis to determine the maximum applicable macrolevel stress.

3. Results

3.1 Stiffness and Strength Properties

Stiffness values have been determined from the modeling and experimental methods just described. Although modeling can quickly predict strength under any loading condition, logistical limitations dictate that experimental tests have been performed to determine strength under uniaxial loading conditions. Though not shown in test-by-test details, each of the experimental tests from table 6 has been repeated for eight specimens. An average value is presented.

Table 6. Experimental and predicted stiffness and strength.

	Description	Experimental (Pa)	Predicted (Pa)	Difference[a] (%)
E_X	*x*-axis stiffness	2.25 e10	2.41 e10	7.3
X_T	*x*-axis strength	5.48 e8	5.65 e8	3.1
E_Y	*y*-axis stiffness	2.26 e10	2.45 e10	8.8
Y_T	*y*-axis strength	4.31 e8	4.96 e8	15.0
G_{XY}	Shear stiffness (in-plane)	4.55 e9	3.95 e9	–13.2
S_{XY}	Shear strength (in-plane)	7.14 e7	5.99 e7	–16.1
G_{XZ}	Transverse shear stiffness	8.93 e9	6.30 e9	–29.5
S_{XZ}	Transverse shear strength	5.76 e8	4.92 e8	–14.5

[a]The mechanical test was performed by P. Moy of ARL, and a separate report will be published.

Per figure 5 and table 1, note that the *x*-direction and *y*-direction geometries are not completely balanced in terms of aligned fiber content. Thus, the properties are slightly different between these two directions. This is also accounted for in the model. However, as seen from comparison of experimental and predicted values, the degree of variation is somewhat underpredicted. In most cases, the model and experimental values show good agreement. In-plane axial and shear properties show an overall average of 90.2% prediction accuracy across strength and stiffness predictions.

Figure 7 shows the *x*-direction microstress state in the RVE under unit extension. As expected, the tows aligned in the loading direction take the bulk of the loading. The transverse stresses that this load case places on the weft tows perpendicular to the load direction often lead to pull-apart or matrix microcracking of the tows. However, ultimate failure is governed by the strength of the warp tows, which still holds stress after the weft tows begin to fail.

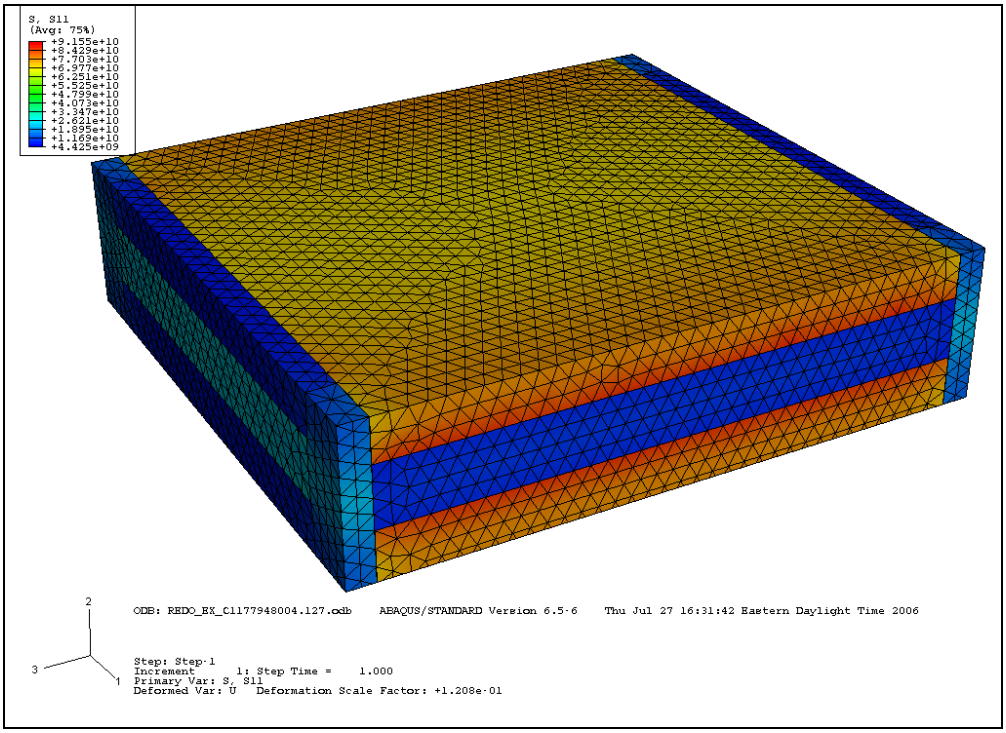

Figure 7. Contour plot illustrating axial stress under unit normal strain along the *x*-direction axis.

Shear stresses in the RVE under unit in-plane shear strain are shown in figure 8. For this planar loading, stresses are much more evenly distributed across the warp and weft tows. The bulk matrix itself is also a significant load carrier, as the inter-tow shear stresses themselves are often governed by the matrix properties (similar to the matrix-driven shear properties of a unidirectional laminated composite).

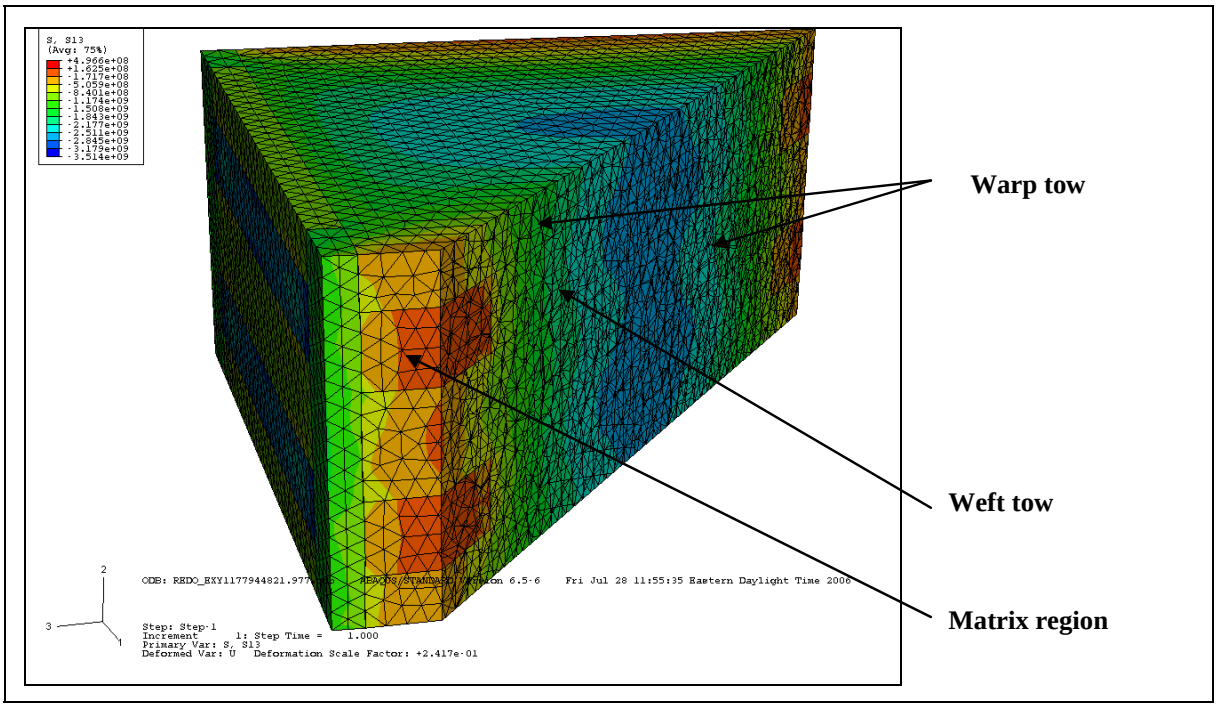

Figure 8. Section-cut contour plot illustrating internal in-plane shear stress under unit shear strain. (Note that two stacked RVEs are shown.)

Transverse shear stiffness is not well predicted, although the model does predict transverse shear strength reasonably well. This is a subject of current work. Even though background derivations have not been developed herein, it should be noted that appropriate boundary conditions to represent transverse shear are not as readily obtainable as those for other deformation states. Thus, the disagreement of model and experiment for this property is not unexpected since some adjustment to the boundary conditions corresponding to transverse shear may be needed.

Nevertheless, strength can still be well predicted. As for a given microstress field, the model can adequately determine the maximum allowables for failure initiation. In short, transverse shear is not a periodic condition because a state of constant transverse shear is always accompanied by a state of nonuniform moment distribution. Thus, if a continuum comprised of RVEs is assembled, each with a uniform transverse shear, the moment present in each RVE across the continuum will vary with length. Periodicity is disrupted, and no single displacement boundary condition can represent what is seen in each RVE. Consequently, the periodic boundary conditions representing the in-plane shear and axial strains (also applicable to flexure states, though not treated in the current work) may not be similarly derived for the transverse shear state.

With the ability to quickly evaluate multiple stress states, the micromechanics model has been used to predict the in-plane failure envelope, as shown in figure 9. This provides a useful “at-a-glance” evaluation of the load capacity of a given material under a variety of applied loads. Also

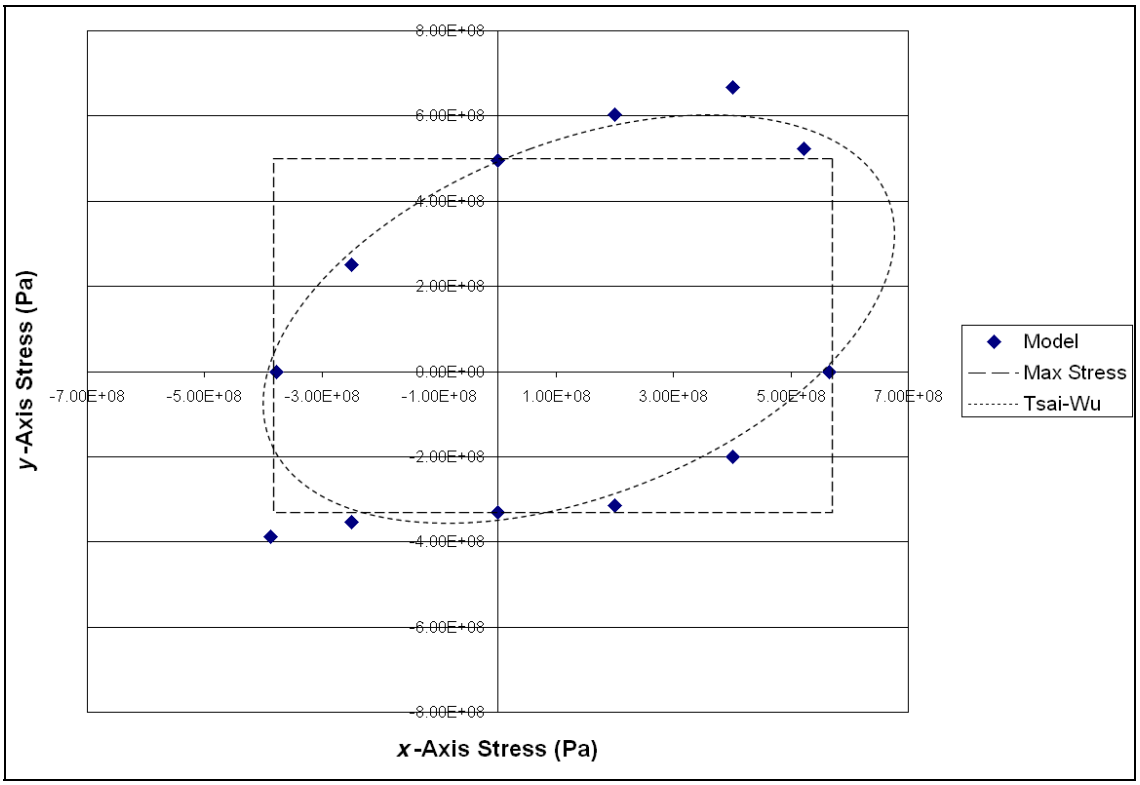

Figure 9. Plane-stress failure envelope with comparison to common failure theories.

shown in figure 9 is a comparison to the predictions of the well-known maximum stress and Tsai-Wu failure theories. All failure theories are inherently formed to agree at the uniaxial failure points (essentially, strength properties). For this relatively simple loading, the general agreement between the Tsai-Wu failure ellipse and the current micromechanics model predictions is fairly close, with most disagreement occurring under the biaxial loading of quadrants I and III. (Note that Tsai-Wu or other common failure theories do not include provision for applied transverse loads or bending moments in their failure prediction, whereas the micromechanics herein can accommodate such considerations.)

Considerable scatter is seen in the results of the off-axis testing—22% and 30% standard deviation for the 30° and 45° specimens, respectively. This is largely due to the inherent inhomogeneity of any textile fiber structure, especially with the relatively sparse through-thickness stitch pattern of the 3-D orthogonal composite. Eight tests were conducted for each of the 30° and 45° specimens to help offset this drift, lend more veracity to the average test result, and maintain validity to comparisons with model predictions. For the 30° specimens, the micromechanics-based model overpredicted the maximum allowable peak load to within 6.4% of the average of the experimental results. With considerably more scatter and two suspect data points, the peak load of the 45° off-axis specimens was overpredicted by the model by 35%. However, if two unreasonably low suspect data points were removed, prediction of the model agreed within 16%

of the experimental data. Given this testing, the micromechanics model allowed effective prediction of failure for this material in simple and relatively more complex load cases.

3.2 Effects of Stitch Density on Stiffness and Strength Properties

Figures 10–14 illustrate the effect of stitch density on the axial and transverse shear stiffness and strength of the 3-D orthogonal composite. Discrete points represent the model predictions, and a solid line indicates a curve fit that has been applied to each plot. An R^2 value is shown on each plot to indicate the relative closeness of each curve fit. Stitch density of 1.6 stitches/cm represents the initial RVE, as shown in figure 1, which is then modified for each new density per the specifications of table 5.

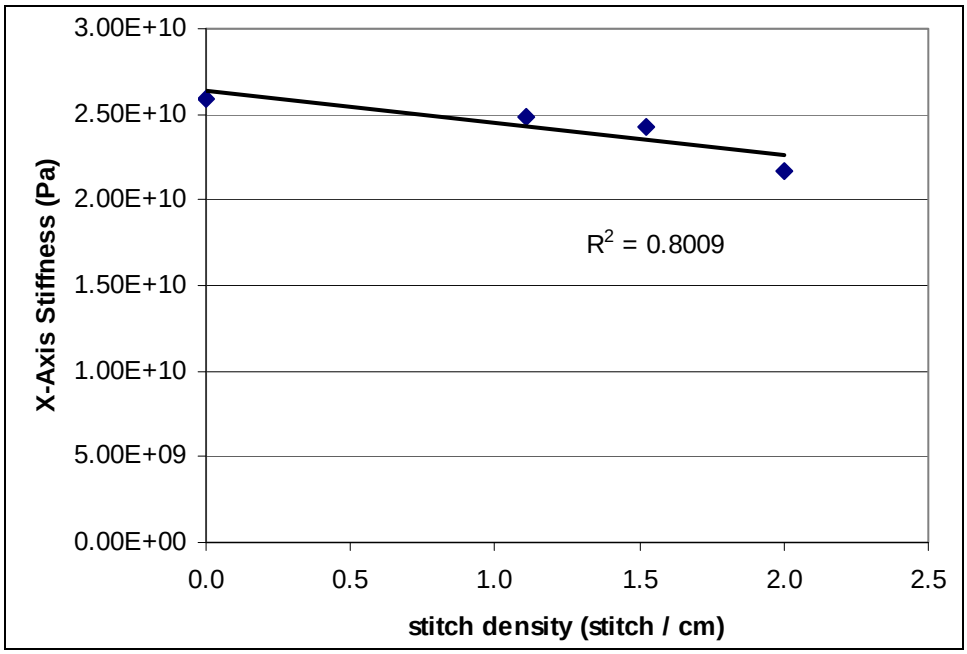

Figure 10. Model predicted effect of stitch density on axial stiffness.

The graphs in figures 10 and 11 present the loss of in-plane axial stiffness and strength for increasing stitch density as predicted via modeling (axial properties in the *y*-direction are not plotted because results compare nearly identically to the *x*-axis properties and thus do not provide new information). Due to the increased presence of interruption of the axial fiber tows which present an in-plane stress concentration and loss of in-plane fiber volume fraction, it is seen that stiffness and strength decrease linearly as stitch density is increased. Linear trends for both property losses follow reasonably well with a "rule of mixtures" relationship or a volume averaging of constituent properties. The results for zero-stitch density have been directly modeled within the FEM but also compare closely to values obtained for a cross-ply laminate analysis in the Classical Laminate Theory (*9*), as the 3-D weave essentially reduces to a cross-ply laminate once the *z*-direction tows are removed.

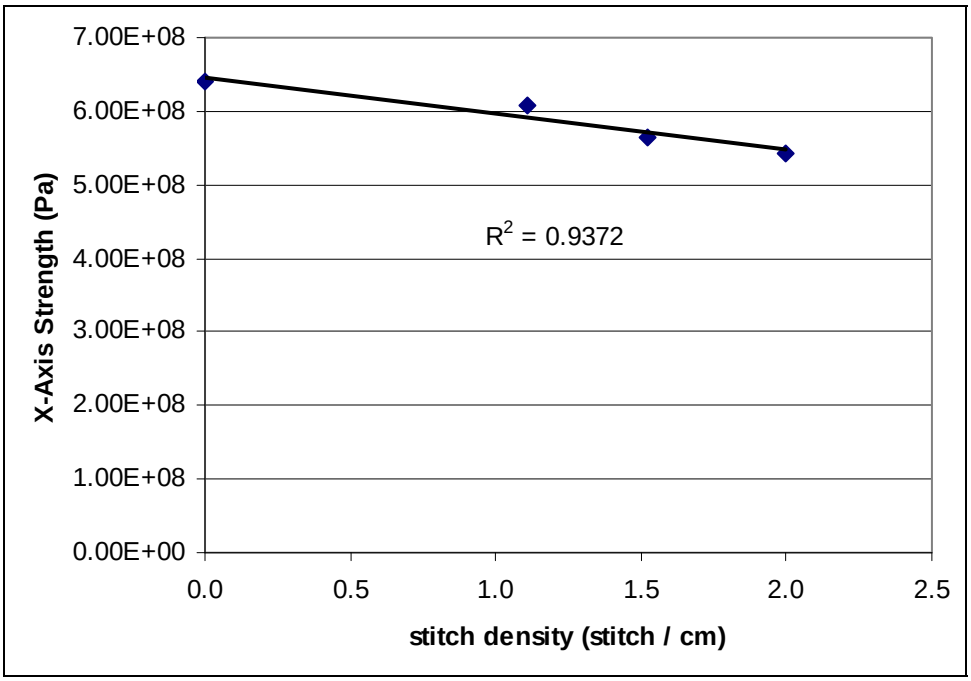

Figure 11. Model predicted effect of stitch density on axial strength.

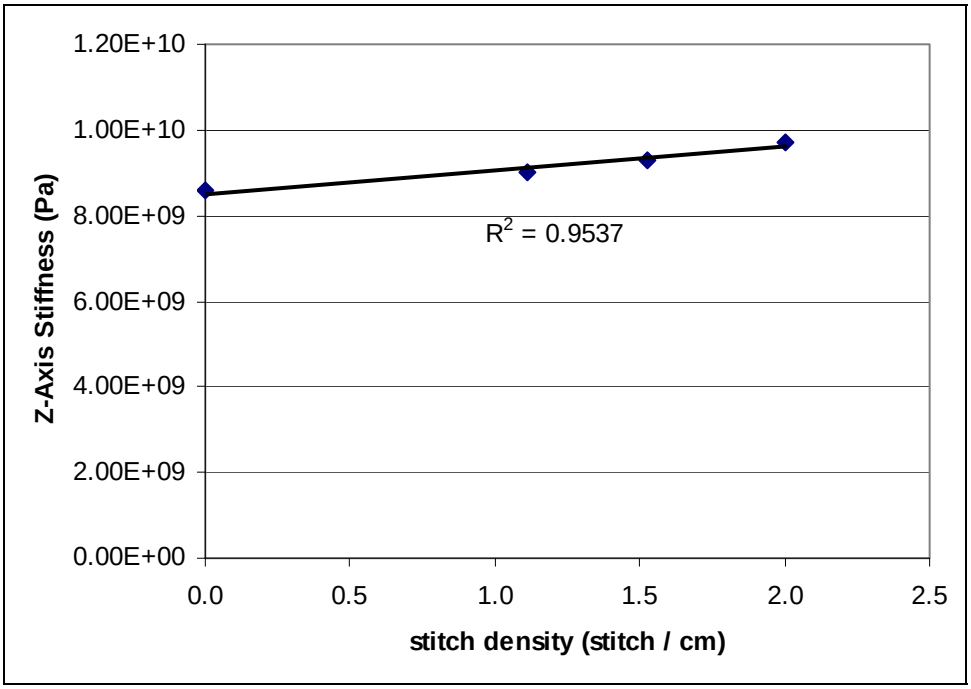

Figure 12. Model predicted effect of stitch density on through-thickness (*z*-axis) stiffness.

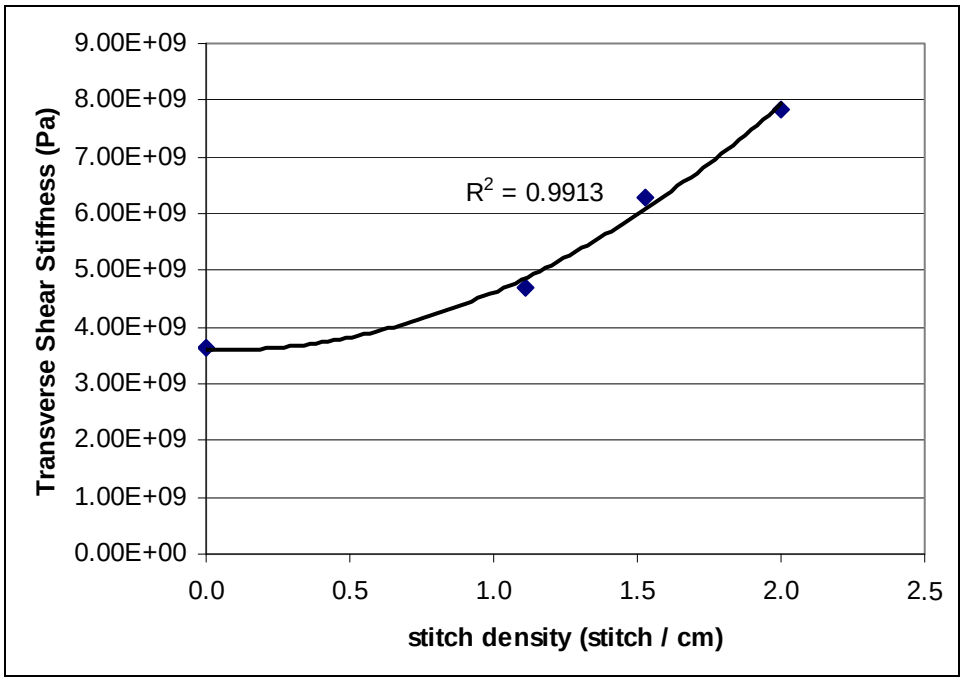

Figure 13. Model predicted effect of stitch density on transverse shear stiffness.

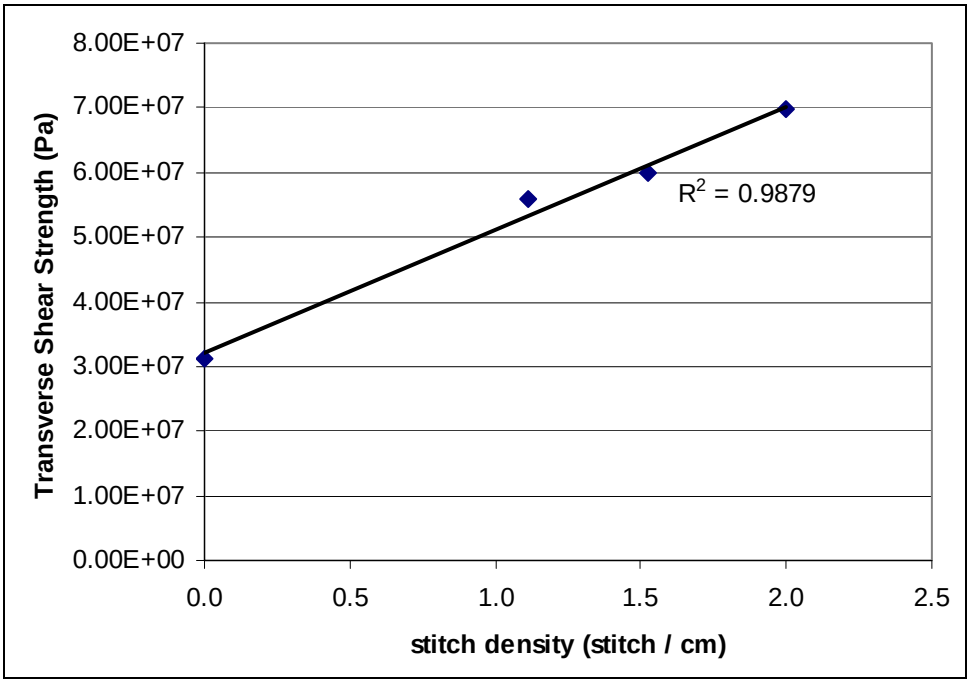

Figure 14. Model predicted effect of stitch density on transverse shear strength.

Figure 12 plots the effect of stitch density on through-thickness stiffness (*z*-direction) of the 3-D weave. In typical applications, stresses in the thickness direction may not be important, even for thick composite parts, but this is a property which is directly affected by stitch density and can represent an important characteristic of structural capability. An increase in stitch density has a direct effect towards increase in through-thickness stiffness. As with the axial properties, this linear trend follows reasonably well with what would be predicted via a rule of mixtures property approximation. A similar plot for through-thickness strength is not shown in the current study due to a present lack of experimental verification of properties and failure modes in this loading condition. An ongoing side study has shown that stitch pullout and tow peeling are the failure modes in this case. Experimental methods for obtaining reliable properties are currently under development.

Figures 13 and 14 show the effect of stitch density on transverse shear properties. Over the selected range of stitch densities, transverse shear properties are the most highly affected by stitch density and can offer 90% or greater gains in stiffness and strength compared to an unstitched sample. This is accompanied by a relatively lower magnitude of loss of in-plane properties on the order of 20%, clearly illustrating the reasoning behind the microgeometry of the 3-D orthogonal weave and showing the value of its employment in impact loading or in thick components.

Although it has been shown that the current micromechanics model predicts transverse shear strength well but does not predict transverse shear stiffness with complete accuracy, the model can be calibrated to fit the experimental data and still accurately predict trends that arise from modification of the RVE microgeometry for the parametric study. Also note that if greater stitch densities were investigated beyond those currently studied, the improvement shown in figure 13 should approach a region of diminishing returns as stitch densities approach volume fractions on the order of the warp and weft tows.

The mechanical response under transverse shear loading is relatively more intricate than for axial or planar shear, as evidenced by the more complex deformation and stress profiles seen under these conditions. Consequently, prediction of these properties is not amenable to simple approximations and must be modeled directly. Changes in transverse shear properties for altered stitch density do not follow the rule of mixtures approximations. Furthermore, properties of the unstitched specimens cannot be compared to predictions from the Classical Laminate Theory because as these methods do not include provisions for calculation of transverse shear properties.

4. Conclusions

In this report, micromechanical methods are used to analyze the failure of a 3-D orthogonal woven textile composite. Photomicrographs of the weave under investigation have allowed the creation of an accurate RVE within the FEM. The micromechanical techniques have been employed to determine the stiffness and strength of the 3-D weave under axial, in-plane shear, and transverse shear loading. In-plane axial and shear properties show an overall average of 90.2% prediction accuracy across strength and stiffness predictions. Transverse shear stiffness is not as well predicted, although the model does predict transverse shear strength reasonably well, with 86% accuracy compared to other experiments. Extending these results, a parametric study has been performed to determine the effect of variation in stitch density upon the consequent mechanical properties. This parametric study, which evaluates the effects of stitch density on mechanical performance, illustrates the potential use of the micromechanics methods as an optimization tool as well as a tool for material investigation and development. In-plane stiffness and strength are somewhat adversely affected by increased stitch density, whereas through-thickness axial properties show improvement. These linear trends could be reasonably well estimated by a rule of mixtures volume-averaging approximation. However, transverse shear properties exhibit a more complex mechanical response, which does not follow simple analytical approximation and must be modeled directly. Over the selected range of stitch densities, transverse shear properties are the most highly affected by stitch density and can offer 90% or greater gains in stiffness and strength compared to an unstitched sample and a 20% relatively lower magnitude of loss of in-plane properties.

5. References

1. Callus, P. J.; Mouritz, A. P.; Bannister, M. K.; Leong, K. H. Tensile Properties and Failure Mechanisms of 3D Woven GRP Composites. *Composites: Part A* **1999**, *30*, 1277–1287.
2. Baucom, J. N.; Zikry, M. A. Evolution of Failure Mechanisms in 2D and 3D Woven Composite Systems Under Quasi-static Perforation. *Journal of Composite Materials* **2003**, *37* (18), 1651–1674.
3. Takeshi, T.; Susuki, I. In-plane and Out-of-plane Characteristics of Three-dimensional Textile Composites. *Journal of Composite Materials* **2005**, *39* (6), 543–556.
4. Baucom, J. N.; Zikry, M. A.; Rajendran, A. M. Low-velocity Impact Damage Accumulation in Woven S2-glass Composite Systems. *Composites Science and Technology* **2006**, *66*, 1229–1238.
5. Valisetty, R.; Rajendran, A. M. Modeling Damage Modes in 3D-woven Armor Composite Systems, *Proceedings of the 25th Army Science Conference*. Orlando, FL, 2006.
6. Yang, B.; Kozey, V.; Adanur, S.; Kumar, S. Bending, Compression, and Shear Behavior of Woven Glass Fiber-epoxy Composites. *Composites: Part B* **2000**, *31*, 715–721.
7. Tarnopol'skii, Y. M.; Kulakov, V. L.; Aranautov, A. K. Measurements of Shear Characteristics of Textile Composites. *Composites and Structures* **2000**, *76*, 115–123.
8. Tsai, S. W.; Hahn, H. T. *Introduction to Composite Materials*; Technomic Publishing Co.: Lancaster, PA, 1980.
9. Gibson, R. F. *Principles of Composite Material Mechanics*; McGraw-Hill, Inc.: New York, 1994.
10. Whitcomb, J. K.; Srirengan, K. Effect of Various Approximations on Predicted Progressive Failure in Plain Weave Composites. *Composite Structures* **1996**, *34*, 13–20.
11. Whitcomb, J. D.; Chapman, C. D.; Srirengan, K. Analysis of Plain-Weave Composites Subjected to Flexure. *Mechanics of Composite Materials and Structures* **1998**, *5*, 41–53.
12. Cox, B. N.; Dadkhah, M. S. A Binary Model of Textile Composites: I- Formulation. *Acta Metallurgica et Materiala* **1994**, *42* (10), 3463.
13. Cox, B. N.; Dadkhah, M. S.; Morris, W. L. On the Tensile Failure of 3D Woven Composites. *Composites: Part A* **1996**, *27*, 447–458.
14. Bogdanovich, A. E.; Pastore, C. M. Material-Smart Analysis of Textile-Reinforced Structures. *Composites Science and Technology* **1996**, *56*, 291–309.

15. Whitney, T. J.; Chou, T. W. Modelling of 3D Angle Interlock Textile Structural Composites. *Journal of Composite Materials* **1989**, *23*, 890.

16. Quek, S. C.; Waas, A. Compressive Response and Failure of Braided Textile Composites: Part 2 - Computations. *International Journal of Nonlinear Mechanics* **2004**, *39*, 649–663.

17. Karkkainen, R. L.; Sankar, B. V. A Direct Micromechanics Method for Failure Initiation of Plain Weave Textile Composites. *Composites Science and Technology* **2006**, *66*, 137–150.

18. Karkkainen, R. L.; Sankar, B. V.; Tzeng, J. T. A Direct Micromechanical Approach Toward the Development of Quadratic Stress Gradient Failure Criteria for Textile Composites. *Journal of Composite Materials*, in press.

19. Karkkainen, R. L.; Sankar, B. V.; Tzeng, J. T. Strength Prediction of Multi-Layer Plain Weave Textile Composites Using the Direct Micromechanics Method. *Composites Part B: Engineering*, in press.

20. Sankar, B. V.; Marrey, R. V. Analytical Method for Micromechanics of Textile Composites. *Composites Science and Technology* **1997**, *57* (6), 703–713.

21. Marrey, R. V.; Sankar, B. V. A Micromechanical Model for Textile Composite Plates. *Journal of Composite Materials* **1997**, *31* (12), 1187–1213.

22. Correlated Solutions, Inc. Home Page. http://www.correlatedsolutions.com (accessed 2005), VIC-3D.

NO. OF COPIES	ORGANIZATION
1 (PDF ONLY)	DEFENSE TECHNICAL INFORMATION CTR DTIC OCA 8725 JOHN J KINGMAN RD STE 0944 FORT BELVOIR VA 22060-6218
1	US ARMY RSRCH DEV & ENGRG CMD SYSTEMS OF SYSTEMS INTEGRATION AMSRD SS T 6000 6TH ST STE 100 FORT BELVOIR VA 22060-5608
1	DIRECTOR US ARMY RESEARCH LAB IMNE ALC IMS 2800 POWDER MILL RD ADELPHI MD 20783-1197
1	DIRECTOR US ARMY RESEARCH LAB AMSRD ARL CI OK TL 2800 POWDER MILL RD ADELPHI MD 20783-1197

ABERDEEN PROVING GROUND

1	DIR USARL AMSRD ARL CI OK TP (BLDG 4600)

NO. OF COPIES ORGANIZATION

2 DIRECTOR
US ARMY RSRCH LAB
AMSRD ARL CI OK T
2800 POWDER MILL RD
ADELPHI MD 20783-1197

1 DIRECTOR
US ARMY RSRCH LAB
AMSRD ARL WM MB
A FRYDMAN
2800 POWDER MILL RD
ADELPHI MD 20783-1197

1 HQDA
DAMI FIT
NOLAN BLDG
WASHINGTON DC 20310-1025

1 COMMANDER
US ARMY MATERIEL CMD
AMXMI INT
9301 CHAPEK RD
FT BELVOIR VA 22060-5527

1 PEO CS&CSS
PM LTV
SFAE CSS LT (M114 MGR)
6501 E ELEVEN MILE RD
WARREN MI 48392-5000

2 NAVAL RESEARCH LAB
CODE 6750
R MEGER
WASHINGTON DC 20375

1 CDR US ARMY TACOM
PM GROUND SYS INTEGRATION
SFAE GCSS W GSI
R LABATILLE
6501 ELEVEN MILE RD
WARREN MI 48397-5000

4 BENET LABS
AMSTA AR CCB
E KATHE
A LITTLEFIELD
J ANDREA
P COTE
WATERVLIET NY 12189

NO. OF COPIES ORGANIZATION

4 US ARMY RSRCH OFC
A CROWSON
D MANN
J PRATER
B LAMATTINA
PO BOX 12211
RSRCH TRIANGLE PARK
NC 27709-2211

1 NSCW
TECH LIBRARY CODE B60
17320 DAHLGREN RD
DAHLGREN VA 22448

3 OFC OF NAVAL RSRCH
E D'ANDREA
R ELLIS
G GRAFF
800 N QUINCY ST
ARLINGTON VA 22217-5660

6 NAVAL SURFACE WARFARE CTR
CODE G33
R HUBBARD
K LEWIS
D BRUNSON
C PETRY
C GARNETT
B MCGLASSON G32
DAHLGREN VA 22448

1 DARPA
B WILCOX
3701 N FAIRFAX DR
ARLINGTON VA 22203-1714

2 DIR LLNL
STEVE DETERESA L-154
MILTON FINGER L-020
PO BOX 808
LIVERMORE CA 94550

3 NASA LANGLEY RSCH CTR
AMSRD ARL VT
F BARTLETT JR
W JACKSON
K O'BRIEN
MS 266
HAMPTON VA 23681-0001

NO. OF COPIES	ORGANIZATION
1	DIR DIA TA 5 K CRELLING WASHINGTON DC 20310
1	US ARMY MISSILE CMD AMSAM RD MG W MCCORKLE REDSTONE ARSENAL AL 35898-5240
3	US ARMY TACOM TARDEC AMSTA TR D A LIJOI M FREEMAN M TOURNER MS 207 WARREN MI 48397-5000
1	US ARMY TACOM ARDEC FSAE GCSS TMA J BENETT BLDG 354 PICATINNY ARSENAL NJ 07806-5000
4	US ARMY ARDEC AMSRD AAR AEE W G COLOMBO LTC FOSTER D LADD R GREENFIELD BLDG 382 PICATINNY ARSENAL NJ 07806-5000
1	US ARMY ARDEC AMSRD AAR AEP M CILLI BLDG 382 PICATINNY ARSENAL NJ 07806-5000
1	NSWC CARDEROCK DIVISION J SOFIA 9500 MACARTHUR BLVD WEST BETHESDA MD 20817-5700
1	SAIC I MAY 8500 NORMANDALE LAKE BLVD STE 1610 BLOOMINGTON MN 55437
10	INST FOR ADVANCED TECH UNIV OF TEXAS AT AUSTIN P SULLIVAN H FAIR M CRAWFORD F BEACH K T HSIEH F STEPHANI I MCNAB S BLESS M ERENGIL S SATAPATHY 3925 W BRAKER LN AUSTIN TX 78759-5316
7	UNIV OF TEXAS AT AUSTIN CTR FOR ELECTROMECHANICS J HAHNE M WERST J BENO J KITZMILLER B RECH J PAPPAS S MANIFOLD PRC MAIL CODE R7000 AUSTIN TX 78712
1	SAIC K A JAMISON PO BOX 4216 FT WALTON BEACH FL 32549
2	IAP RESEARCH INC D BAUER J BARBER 2763 CULVER AVE DAYTON OH 45429-3723
3	CURTISS-WRIGHT EMD M DEMBRAK K BERTON J HILLENBRAND CHESWICK PA 15024-1300
2	DEPUTY ASST SECY FOR R&T SARD TT T KILION J PARMENTOLA RM 3EA79 THE PENTAGON WASHINGTON DC 20301-7100

NO. OF COPIES ORGANIZATION

1 GENERAL ATOMICS
T HURN
3550 GENERAL ATOMICS CT
SAN DIEGO CA 92121

1 BAE SYS ARMAMENT SYS
A CHABOKI
4800 E RIVER RD
MINNEAPOLIS MN 55421-1498

ABERDEEN PROVING GROUND

62 DIR USARL
AMSRD ARL SE D
E SHAFFER
AMSRD ARL WM
A ALTHOUSE
S KARNA
J MCCAULEY
J SMITH
T WRIGHT
AMSRD ARL WM SG
R CARTER
T ROSENBERGER
AMSRD ARL WM B
C CANDLAND
M ZOLTOSKI
AMSRD ARL WM BA
T KOGLER
D LYON
AMSRD ARL WM BC
J NEWILL
AMSRD ARL WM BD
B FORCH
R LIEB
A ZIELINSKI
AMSRD ARL WM RP
C SHOEMAKER
AMSRD ARL EG
E SCHMIDT
AMSRD ARL WM M
J BEATTY
R DOWDING
S MCKNIGHT

NO. OF COPIES ORGANIZATION

AMSRD ARL WM MA
R JENSEN
P MOY
D O'BRIEN
M VANLANDINGHAM
E WETZEL
AMSRD ARL WM MB
J BENDER
T BOGETTI
L BURTON
W DRYSDALE
R EMERSON
D HOPKINS
R KASTE
T LI
J SOUTH
T TZENG (5 CPS)
AMSRD ARL WM MC
V CHAMPAGNE
D GRANVILLE
M MAHER
W SPURGEON
AMSRD ARL WM MD
C CHIN
K CHO
P DEHMER
R DOOLEY
S GHIORSE
G GILDE
J SANDS
D SPAGNUOLO
S WALSH
AMSRD ARL WM T
P BAKER
B BURNS
AMSRD ARL WM TA
W BRUCHEY
W GILLICH
C HOPPEL
M KEELE
S SCHOENFELD
AMSRD ARL WM TC
R COATES
B SORENSEN
AMSRD ARL WM TE
J POWELL

INTENTIONALLY LEFT BLANK.